

FAST-LIO: A Fast, Robust LiDAR-inertial Odometry Package by Tightly-Coupled Iterated Kalman Filter

Wei Xu¹, Fu Zhang¹

Abstract—This paper presents a computationally efficient and robust LiDAR-inertial odometry framework. We fuse LiDAR feature points with IMU data using a tightly-coupled iterated extended Kalman filter to allow robust navigation in fast-motion, noisy or cluttered environments where degeneration occurs. To lower the computation load in the presence of large number of measurements, we present a new formula to compute the Kalman gain. The new formula has computation load depending on the state dimension instead of the measurement dimension. The proposed method and its implementation are tested in various indoor and outdoor environments. In all tests, our method produces reliable navigation results in real-time: running on a quadrotor onboard computer, it fuses more than 1,200 effective feature points in a scan and completes all iterations of an iEKF step within 25 *ms*. Our codes are open-sourced online².

I. INTRODUCTION

Simultaneous localization and mapping (SLAM) is a fundamental prerequisite of mobile robots, such as unmanned aerial vehicles (UAVs). Visual (-inertial) odometry (VO), such as Stereo VO [1, 2] and Monocular VO [3, 4] are commonly used on mobile robots due to its lightweight and low-cost. Although providing rich RGB information, visual solutions lack direct depth measurements and require much computation resources to reconstruct the 3D environment for trajectory planning. Moreover, they are very sensitive to lighting conditions. Light detection and ranging (LiDAR) sensors could overcome all these difficulties but have been too costly (and bulky) for small-scale mobile robots.

Solid-state LiDARs recently emerge as main trends in LiDAR developments, such as those based on micro-electro-mechanical-system (MEMS) scanning [5] and rotating prisms [6]. These LiDARs are very cost-effective (in a cost range similar to global shutter cameras), lightweight (can be carried by a small-scale UAV), and of high performance (producing active and direct 3D measurements of long-range and high-accuracy). These features make such LiDARs viable for UAVs, especially industrial UAVs which need to acquire accurate 3D maps of the environments (e.g., aerial mapping) or may operate in cluttered environments with severe illumination variations (e.g., post-disaster search and inspection).

Despite the great potentiality, solid-state LiDARs bring new challenges to SLAM: 1) the feature points in LiDAR measurements are usually the geometrical structures (e.g. edges and planes) in the environments. When the UAV is

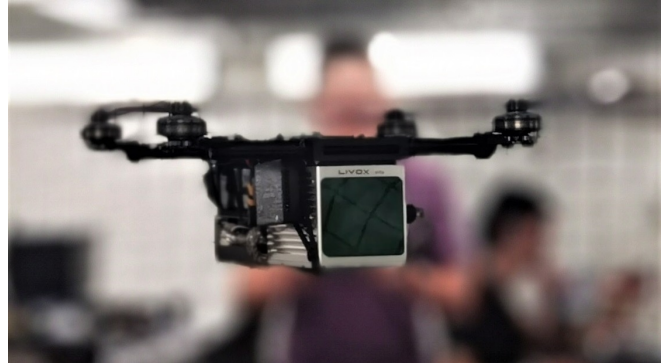


Fig. 1. Our LiDAR-inertial navigation system runs on a Livox AVIA LiDAR³ and a DJI Manifold 2-C computer⁴, all on a customized small-scale quadrotor UAV (280 *mm* wheelbase).

operating in cluttered environments where no strong features are present, the LiDAR-based solution easily degenerates. This problem is more obvious when the LiDAR has small FoV. 2) Due to the high-resolution along the scanning direction, a LiDAR scan usually contains many feature points (e.g. a few thousands). While these feature points are not adequate to reliably determine the pose in case of degeneration, tightly fusing such large number of feature points to IMU measurements requires tremendous computation resources that are not affordable by the UAV onboard computer. 3) Since the LiDAR samples points sequentially with a few laser/receiver pairs, laser points in a scan are always sampled at different times, resulting in motion distortion that will significantly degrade a scan registration [7]. The constant rotations of UAV propellers and motors also introduce significant noises to the IMU measurements.

To make the LiDAR navigation viable for small-scale mobile robots such as UAVs, we propose the FAST-LIO, a computationally efficient and robust LiDAR-inertial odometry package. More specifically, our contributions are as follows: 1) To cope with fast-motion, noisy or cluttered environments where degeneration occurs, we adopt a tightly-coupled iterated Kalman filter to fuse LiDAR feature points with IMU measurements. We propose a formal back-propagation process to compensate the motion distortion; 2) To lower the computation load caused by large number of LiDAR feature points, we propose a new formula for computing the Kalman gain and proved its equivalence to the conventional

¹All authors are with Department of Mechanical Engineering, University of Hong Kong. {xuwei1, fuzhang}@hku.hk

²<https://github.com/hku-mars/FAST-LIO>

³<https://www.uav.org/dji-drone-LiDAR-introducing-livox-and-avia/>

⁴<https://www.dji.com/cn/manifold-2/specs>

Kalman gain formula. The new formula has a computation complexity depending on the state dimension instead of measurements dimension. 3) We implement our formulations into a fast and robust LiDAR-inertial odometry software package. The system is able to run on a small-scale quadrotor onboard computer. 4) We conduct experiments in various indoor and outdoor environments and with actual UAV flight tests (Fig. 1) to validate the system robustness when fast motion or intense vibration noise exists.

The remaining paper is organized as follows: In Section. II, we discuss relevant research works. We give an overview of the complete system pipeline and the details of each key components in Section. III. The experimental results are presented in Section. IV, followed by conclusions in Section. V.

II. RELATED WORKS

Existing works on LiDAR SLAM are extensive, and a full review would be too time-consuming nor necessary. Hence we limit our review to the most relevant work: LiDAR only odometry and mapping, loosely coupled and tightly coupled LiDAR-Inertial fusion methods.

A. LiDAR Odometry and Mapping

Besl *et al* [7] propose an iterated closest points (ICP) method for scan registration, which builds the basis for LiDAR odometry. ICP performs well for dense 3D scans. However, for sparse point cloud of LiDAR measurements, the exact point matching required by ICP rarely exists. To cope with this problem, Segal *et al* [8] propose a generalized-ICP based on the point-to-plane distance. Then Zhang *et al* [9] combine this ICP method with a point-to-edge distance and developed a LiDAR odometry and mapping (LOAM) framework. Thereafter, many variants of LOAM have been developed, such as LeGO-LOAM [10] and LOAM-Livox [11]. While these methods work well for structured environments and LiDARs of large FoV, they are very vulnerable to featureless environments or small FoV LiDARs [11].

B. Loosely-coupled LiDAR-Inertial Odometry

IMU measurements are commonly used to mitigate the problem of LiDAR degeneration in featureless environments. Loosely-coupled LiDAR-inertial odometry (LIO) methods typically process the LiDAR and IMU measurements separately and fuse their results later. For example, IMU-aided LOAM [9] takes the pose integrated from IMU measurements as the initial estimate for LiDAR scan registration. Zhen *et al* [12] fuse the IMU measurements and the Gaussian Particle Filter output of LiDAR measurements using the error-state EKF. Balazadegan *et al* [13] add the IMU-gravity model to estimate the 6-DOF ego-motion to aid the LiDAR scan registration. Zuo *et al* [14] use a Multi-State Constraint Kalman Filter (MSCKF) to fuse the scan registration results with IMU and visual measurements. A common procedure of the loosely-coupled approach is obtaining a pose measurement by registering a new scan and then fusing the pose measurement with IMU measurements. The separation between

scan registration and data fusion reduces the computation load. However, it ignores the correlation between the system other states (e.g., velocity) and the pose of the new scan. Moreover, in the case of featureless environments, the scan registration could degenerate in certain directions and causes unreliable fusion in later stages.

C. Tightly-coupled LiDAR-Inertial Odometry

Unlike the loosely-coupled methods, tightly-coupled LiDAR-inertial odometry methods typically fuse the raw feature points (instead of scan registration results) of LiDAR with IMU data. There are two main approaches to tightly-coupled LIO: optimization-based and filter-based. Geneva *et al* [15] use a graph optimization with IMU pre-integration constrains [16] and plane constrains [17] from LiDAR feature points. Recently, Ye *et al* [18] propose the LIOM package which uses a similar graph optimization but is based on edge and plane features. For filter-based methods, Bry [19] uses a Gaussian Particle Filter (GPF) to fuse the data of IMU and a planar 2D LiDAR. This method has also been used in the Boston Dynamics Atlas humanoid robot. Since the computation complexity of particle filter grows quickly with the number of LiDAR points and the system dimension, Kalman filter and its variants are usually more preferred, such as extended Kalman filter [20], unscented Kalman filter [21], and iterated Kalman filter [22].

Our method falls into the tightly-coupled approach. We adopt an iterated extended Kalman filter similar to [22] to mitigate linearization errors. Kalman filter (and its variants) has a time complexity $\mathcal{O}(m^2)$ where m is the measurement dimension [23], this may lead to remarkably high computation load when dealing with a large number of LiDAR measurements. Naïve down-sampling would reduce the number of measurements, but at the cost of information loss. [22] reduces the number of measurements by extracting and fitting ground planes similar to [10]. This, however, does not apply to aerial applications where the ground plane may not always be present.

III. METHODOLOGY

A. Framework Overview

The overview of our workflow is shown in Fig. 2. The LiDAR inputs are fed into the feature extraction module to obtain the planar and edge features following the methods in LOAM [9]. Then the extracted features and IMU measurements are fed into an iterated Kalman filter based state estimator. The state estimator interact with the global map which contains all the history features and output the real-time odometry. When each states estimation finished, the map will also be updated with the new features. The state estimator will be detailed described in Section III-C.

B. System Description

1) Continuous model:

Assuming an IMU is rigidly attached to the LiDAR with a known extrinsic ${}^L\mathbf{T}_L = ({}^L\mathbf{R}_L, {}^L\mathbf{p}_L)$. Taking the IMU

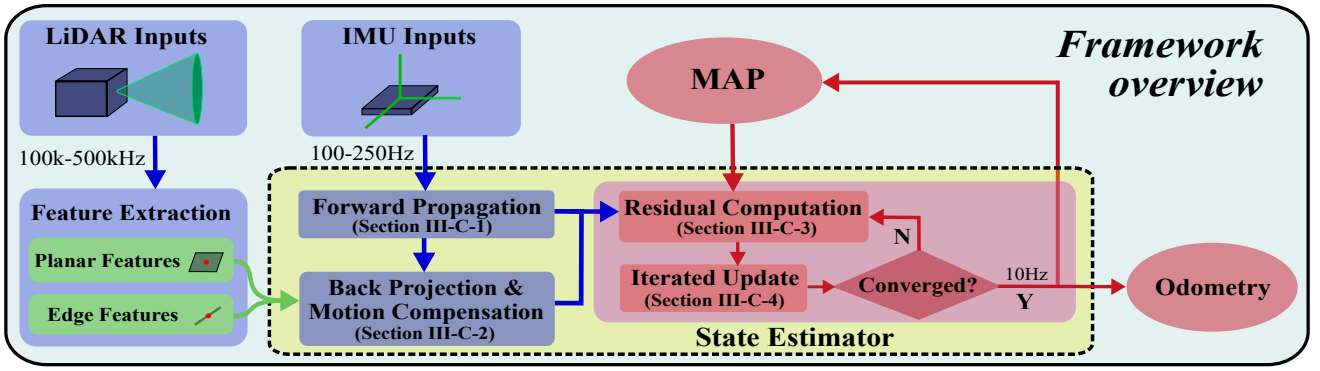


Fig. 2. System overview of FAST-LIO.

frame (denoted as I) as the body frame of reference leads to a kinematic model:

$$\begin{aligned} {}^G\dot{\mathbf{p}}_I &= {}^G\mathbf{v}_I, \quad {}^G\dot{\mathbf{v}}_I = {}^G\mathbf{R}_I (\mathbf{a}_m - \mathbf{b}_a - \mathbf{n}_a) + {}^G\mathbf{g}, \quad {}^G\dot{\mathbf{g}} = \mathbf{0} \\ {}^G\dot{\mathbf{R}}_I &= {}^G\hat{\mathbf{R}}_I [\boldsymbol{\omega}_m - \mathbf{b}_\omega - \mathbf{n}_\omega]_\wedge, \quad \dot{\mathbf{b}}_\omega = \mathbf{n}_{b\omega}, \quad \dot{\mathbf{b}}_a = \mathbf{n}_{ba} \end{aligned} \quad (1)$$

where ${}^G\mathbf{p}_I$, ${}^G\mathbf{R}_I$ are the position and attitude of IMU in the global frame (i.e., the first IMU frame, denoted as G), ${}^G\mathbf{g}$ is the unknown gravity vector in the global frame, \mathbf{a}_m and $\boldsymbol{\omega}_m$ are IMU measurements, \mathbf{n}_a and \mathbf{n}_ω are the white noise of IMU measurements, \mathbf{b}_a and \mathbf{b}_ω are the IMU bias modelled as the random walk process with Gaussian noises \mathbf{n}_{ba} and $\mathbf{n}_{b\omega}$, and the notation $[\mathbf{a}]_\wedge$ denotes the skew-symmetric matrix of vector $\mathbf{a} \in \mathbb{R}^3$.

2) Discrete model:

Based on the \boxplus operation defined in [24], we can discretize the continuous model in (1) at the IMU sampling period Δt using a zero-order holder. The resultant discrete model is

$$\mathbf{x}_{i+1} = \mathbf{x}_i \boxplus (\Delta t \mathbf{f}(\mathbf{x}_i, \mathbf{u}_i, \mathbf{w}_i)) \quad (2)$$

where the function \mathbf{f} , state \mathbf{x} , inputs \mathbf{u} and noise vector \mathbf{w} are defined as below:

$$\begin{aligned} \mathbf{x} &\doteq [{}^G\mathbf{R}_I^T \quad {}^G\mathbf{p}_I^T \quad {}^G\mathbf{v}_I^T \quad \mathbf{b}_\omega^T \quad \mathbf{b}_a^T \quad {}^G\mathbf{g}^T]^T \\ \mathbf{u} &\doteq [\boldsymbol{\omega}_m^T \quad \mathbf{a}_m^T]^T, \quad \mathbf{w} \doteq [\mathbf{n}_\omega^T \quad \mathbf{n}_a^T \quad \mathbf{n}_{b\omega}^T \quad \mathbf{n}_{ba}^T]^T \\ \mathbf{f}(\mathbf{x}_k, \mathbf{u}_k, \mathbf{w}_k) &= \begin{bmatrix} \boldsymbol{\omega}_{m_k} - \mathbf{b}_{\omega_k} - \mathbf{n}_{\omega_k} \\ {}^G\mathbf{v}_{I_k} \\ {}^G\mathbf{R}_{I_k} (\mathbf{a}_{m_k} - \mathbf{b}_{a_k} - \mathbf{n}_{a_k}) + {}^G\mathbf{g}_k \\ \mathbf{n}_{b\omega_k} \\ \mathbf{n}_{ba_k} \\ \mathbf{0}_{3 \times 1} \end{bmatrix} \end{aligned} \quad (3)$$

3) Measurement model:

The measurements are feature points from the feature extraction module. Since the lidar points are at a very high sample rate (e.g., 200kHz), it is usually not possible to process each new point once being received. A more practical approach is to accumulate these points for a certain time and process them all at once. Such an accumulated set of points is called a scan and the time for processing it is denoted as t_k (see Fig. 3). During a lidar scan, there are multiple IMU

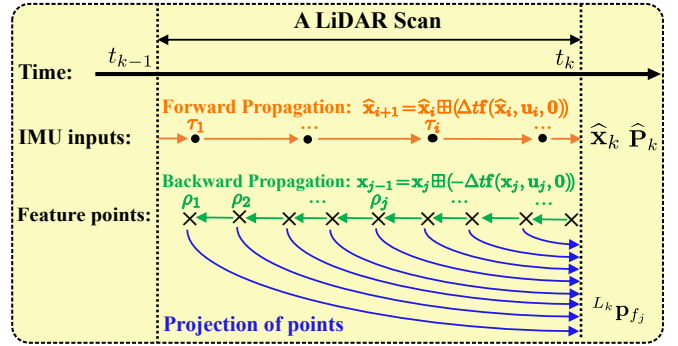


Fig. 3. The procedures of forward propagation, backward propagation and points projection in a LiDAR scan.

measurements, each sampled at time $\tau_i \in [t_{k-1}, t_k]$ with the respective state \mathbf{x}_i as in (2). There are also many feature points in a scan. Assume the number of feature points is m , each is sampled at time $\rho_j \in [t_{k-1}, t_k]$ and is denoted as $L_j \mathbf{p}_{f_j}$, where L_j is the lidar frame at the time ρ_j .

C. States Estimator

To estimate the states in the state formulation (2), we use an iterated extended Kalman filter. Moreover, we characterize the estimation covariance in the tangent space of the state estimate as in [24, 25]. Assume the optimal state estimate of the last lidar scan at t_{k-1} is $\bar{\mathbf{x}}_{k-1}$ with covariance matrix $\bar{\mathbf{P}}_{k-1}$. Then $\bar{\mathbf{P}}_{k-1}$ represents the covariance of the random error state vector defined below:

$$\tilde{\mathbf{x}}_{k-1} \doteq \mathbf{x}_{k-1} \boxminus \bar{\mathbf{x}}_{k-1} = \begin{bmatrix} \delta\boldsymbol{\theta}^T & {}^G\tilde{\mathbf{p}}_I^T & {}^G\tilde{\mathbf{v}}_I^T & \tilde{\mathbf{b}}_\omega^T & \tilde{\mathbf{b}}_a^T & {}^G\tilde{\mathbf{g}}^T \end{bmatrix}^T \quad (4)$$

where $\delta\boldsymbol{\theta} = \text{Log}({}^G\tilde{\mathbf{R}}_I^T {}^G\mathbf{R}_I)$ is the attitude error and the rests are standard additive errors (i.e., the error in the estimate $\tilde{\mathbf{x}}$ of a quantity \mathbf{x} is $\tilde{\mathbf{x}} = \mathbf{x} - \bar{\mathbf{x}}$). Intuitively, the attitude error $\delta\boldsymbol{\theta}$ describes the (small) deviation between the true and the estimated attitude. The main advantage of this error definition is that it allows us to represent the attitude uncertainty by the 3×3 covariance matrix $\mathbb{E}\{\delta\boldsymbol{\theta}\delta\boldsymbol{\theta}^T\}$. Since the attitude has 3 degree of freedom (DOF), this is a minimal representation.

1) Forward Propagation:

$$\mathbf{F}_{\bar{\mathbf{x}}} = \begin{bmatrix} \text{Exp}(-\hat{\omega}_i \Delta t) & \mathbf{0} & \mathbf{0} & -\mathbf{A}(\hat{\omega}_i \Delta t)^T \Delta t & \mathbf{0} & \mathbf{0} \\ \mathbf{0} & \mathbf{I} & \mathbf{I} \Delta t & \mathbf{0} & \mathbf{0} & \mathbf{0} \\ -{}^G \hat{\mathbf{R}}_{I_i} [\hat{\mathbf{a}}_i]_{\wedge} \Delta t & \mathbf{0} & \mathbf{I} & \mathbf{0} & -{}^G \hat{\mathbf{R}}_{I_i} \Delta t & \mathbf{I} \Delta t \\ \mathbf{0} & \mathbf{0} & \mathbf{0} & \mathbf{I} & \mathbf{0} & \mathbf{0} \\ \mathbf{0} & \mathbf{0} & \mathbf{0} & \mathbf{0} & \mathbf{I} & \mathbf{0} \\ \mathbf{0} & \mathbf{0} & \mathbf{0} & \mathbf{0} & \mathbf{0} & \mathbf{I} \end{bmatrix}, \mathbf{F}_{\mathbf{w}} = \begin{bmatrix} -\mathbf{A}(\hat{\omega}_i \Delta t)^T \Delta t & \mathbf{0} & \mathbf{0} & \mathbf{0} \\ \mathbf{0} & \mathbf{0} & \mathbf{0} & \mathbf{0} \\ \mathbf{0} & -{}^G \hat{\mathbf{R}}_{I_i} \Delta t & \mathbf{0} & \mathbf{0} \\ \mathbf{0} & \mathbf{0} & \mathbf{I} \Delta t & \mathbf{0} \\ \mathbf{0} & \mathbf{0} & \mathbf{0} & \mathbf{I} \Delta t \\ \mathbf{0} & \mathbf{0} & \mathbf{0} & \mathbf{0} \end{bmatrix} \quad (7)$$

The forward propagation is performed once receiving an IMU input (see Fig. 3). More specifically, the state is propagated following (2) by setting the process noise \mathbf{w}_i to zero:

$$\hat{\mathbf{x}}_{i+1} = \hat{\mathbf{x}}_i \boxplus (\Delta t \mathbf{f}(\hat{\mathbf{x}}_i, \mathbf{u}_i, \mathbf{0})); \hat{\mathbf{x}}_0 = \bar{\mathbf{x}}_{k-1}. \quad (5)$$

To propagate the covariance, we use the error state dynamic model obtained below:

$$\begin{aligned} \tilde{\mathbf{x}}_{i+1} &= \mathbf{x}_{i+1} \boxminus \hat{\mathbf{x}}_{i+1} \\ &= (\mathbf{x}_i \boxplus \Delta t \mathbf{f}(\mathbf{x}_i, \mathbf{u}_i, \mathbf{w}_i)) \boxminus (\hat{\mathbf{x}}_i \boxplus \Delta t \mathbf{f}(\hat{\mathbf{x}}_i, \mathbf{u}_i, \mathbf{0})) \\ &\stackrel{(25)}{\simeq} \mathbf{F}_{\tilde{\mathbf{x}}} \tilde{\mathbf{x}}_i + \mathbf{F}_{\mathbf{w}} \mathbf{w}_i. \end{aligned} \quad (6)$$

The matrix $\mathbf{F}_{\tilde{\mathbf{x}}}$ and $\mathbf{F}_{\mathbf{w}}$ in (6) is computed following the Appendix. A. The result is shown in (7). Denoting the covariance of white noises \mathbf{w} as \mathbf{Q} , then the propagated covariance $\hat{\mathbf{P}}_i$ can be computed iteratively following the below equation.

$$\hat{\mathbf{P}}_{i+1} = \mathbf{F}_{\tilde{\mathbf{x}}} \hat{\mathbf{P}}_i \mathbf{F}_{\tilde{\mathbf{x}}}^T + \mathbf{F}_{\mathbf{w}} \mathbf{Q} \mathbf{F}_{\mathbf{w}}^T; \hat{\mathbf{P}}_0 = \bar{\mathbf{P}}_{k-1}. \quad (8)$$

The propagation continues until reaching a new scan of feature points at t_k where the propagated state and covariance are denoted as $\hat{\mathbf{x}}_k, \hat{\mathbf{P}}_k$. Then $\hat{\mathbf{P}}_k$ represents the covariance of the error between the ground-truth state \mathbf{x}_k and the state propagation $\hat{\mathbf{x}}_k$ (i.e., $\mathbf{x}_k \boxminus \hat{\mathbf{x}}_k$).

2) Backward Propagation and Motion Compensation:

When certain number (or time) of feature points are accumulated into a new scan at time t_k , the new scan of feature points should be fused with the propagated state $\hat{\mathbf{x}}_k$ and covariance $\hat{\mathbf{P}}_k$ to produce an optimal state update. However, although the new scan is at time t_k , the feature points are measured at their respective sampling time $\rho_j < t_k$ (see Section. III-B.3), causing a mismatch in the body frame of reference.

To compensate the relative motion (i.e., motion distortion) between time ρ_j and time t_k , we propagate (2) backward as $\mathbf{x}_{j-1} = \mathbf{x}_j \boxminus (-\Delta t \mathbf{f}(\mathbf{x}_j, \mathbf{u}_j, \mathbf{0}))$ backwards, starting from zero pose and rests states (e.g., velocity and bias) from $\hat{\mathbf{x}}_k$. The backward propagation is performed at the frequency of lidar point rate, which is usually much higher than the IMU rate. Back propagating the full state in (2) is time-consuming due to the high point rate. In practice, we need only to back-propagate the pose. Moreover, due to the constant angular speed during two IMU measurements, back-propagating the pose between two IMU measurements can be computed in

a closed-form solution. The resultant back-propagation is usually very fast.

The backward propagation will produce a relative pose between time ρ_j and scan-end time t_k : ${}^{I_k} \hat{\mathbf{T}}_{I_j} = ({}^{I_k} \hat{\mathbf{R}}_{I_j}, {}^{I_k} \hat{\mathbf{p}}_{I_j})$. This relative pose enables us to project the local measurement ${}^{L_j} \mathbf{p}_{f_j}$ to scan-end measurement ${}^{L_k} \mathbf{p}_{f_j}$ as follows (see Fig. 3):

$${}^{L_k} \mathbf{p}_{f_j} = {}^I \mathbf{T}_L^{-1} {}^{I_k} \hat{\mathbf{T}}_{I_j} {}^I \mathbf{T}_L {}^{L_j} \mathbf{p}_{f_j}, \quad (9)$$

where ${}^I \mathbf{T}_L$ is the known extrinsic (see Section. III-B.1). Then the projected point ${}^{L_k} \mathbf{p}_{f_j}$ is used to construct a residual in the following section.

3) Residual computation:

With the motion compensation in (9), we can view the scan of feature points $\{{}^{L_k} \mathbf{p}_{f_j}\}$ all sampled at the same time t_k and use it to construct the residual. Assume the current iteration of the iterated Kalman filter is κ , and the corresponding state estimate at t_k is $\hat{\mathbf{x}}_k^\kappa$. When $\kappa = 0$, $\hat{\mathbf{x}}_k^\kappa = \hat{\mathbf{x}}_k$, the predicted state from the propagation in (5). Then, the feature points $\{{}^{L_k} \mathbf{p}_{f_j}\}$ sampled at time t_k can be projected to the global frame as below:

$${}^G \hat{\mathbf{p}}_{f_j}^\kappa = {}^G \hat{\mathbf{T}}_{I_k}^\kappa {}^I \mathbf{T}_L {}^{L_k} \mathbf{p}_{f_j}; j = 1, \dots, m. \quad (10)$$

With the coordinate in the global frame ${}^G \hat{\mathbf{p}}_{f_j}$, we can search for the corresponding plane (or edge) in the existing map following the method in [11]. Denoting \mathbf{u}_j the normal vector (or edge orientation) of corresponding plane (or edge), on which lying a point ${}^G \mathbf{q}_j$, then this feature point contributes a residual \mathbf{z}_j as below:

$$\mathbf{z}_j^\kappa = \mathbf{G}_j \left({}^G \hat{\mathbf{p}}_{f_j}^\kappa - {}^G \mathbf{q}_j \right), \quad (11)$$

where $\mathbf{G}_j = \mathbf{u}_j^T$ for planar features and $\mathbf{G}_j = [\mathbf{u}_j]_{\wedge}$ for edge features.

4) Iterated update:

To fuse the residual \mathbf{z}_j^κ computed in (11) with the state prediction $\hat{\mathbf{x}}_k$ and covariance $\hat{\mathbf{P}}_k$ propagated from the IMU data, we need to linearize the measurement model that relates the measurements \mathbf{z}_j^κ to the ground-truth state \mathbf{x}_k and measurement noise. The measurement noise originates from the lidar point noise ${}^{L_j} \mathbf{n}_{f_j}$ when measuring each raw feature point ${}^{L_j} \mathbf{p}_{f_j}$. Compensating this measuring noise in the raw feature point leads to the ground-truth measurement

$${}^{L_j} \mathbf{p}_{f_j}^{\text{gt}} = {}^{L_j} \mathbf{p}_{f_j} + {}^{L_j} \mathbf{n}_{f_j}. \quad (12)$$

Assume the relative pose ${}^{I_k}\widehat{\mathbf{T}}_{I_j}$ obtained from the back propagation is accurate, then the ground-truth measurement in (12) when compensated the ground-truth state \mathbf{x}_k should lie exactly on the plane (or edge). That is, plugging (12) into (9), then into (10), and further into (10) should result in zero. i.e.,

$$\mathbf{0} = \mathbf{h}_j(\mathbf{x}_k) = \mathbf{G}_j \left({}^G\mathbf{T}_{I_k} {}^{I_k}\widehat{\mathbf{T}}_{I_j} {}^I\mathbf{T}_L ({}^{L_j}\mathbf{p}_{f_j} + {}^{L_j}\mathbf{n}_{f_j}) - {}^G\mathbf{q}_j \right). \quad (13)$$

Approximating the above equation by its first order approximation made at $\widehat{\mathbf{x}}_k^\kappa$ leads to

$$\mathbf{0} = \mathbf{h}_j(\mathbf{x}_k) \simeq \mathbf{z}_j^\kappa + \mathbf{H}_j^\kappa \widetilde{\mathbf{x}}_k^\kappa + \mathbf{v}_j, \quad (14)$$

where \mathbf{H}_j^κ is the Jacobin matrix of $\mathbf{h}_j(\mathbf{x})$ in (13) with respect to \mathbf{x} , evaluated at $\widehat{\mathbf{x}}_k^\kappa$, $\widetilde{\mathbf{x}}_k^\kappa$ is the error between \mathbf{x}_k and $\widehat{\mathbf{x}}_k^\kappa$, and $\mathbf{v}_j \in \mathcal{N}(\mathbf{0}, \mathbf{R}_j)$ comes from the raw measurement noise ${}^{L_j}\mathbf{n}_{f_j}$ in (13).

Notice that the prior distribution of \mathbf{x}_k obtained from the forward propagation in Section. III-C.1 is for

$$\mathbf{x} \boxminus \widehat{\mathbf{x}}_k = (\widehat{\mathbf{x}}_k^\kappa \boxminus \widehat{\mathbf{x}}_k^\kappa) \boxminus \widehat{\mathbf{x}}_k = \mathbf{J}(\widehat{\mathbf{x}}_k^\kappa \boxminus \widehat{\mathbf{x}}_k^\kappa) \widetilde{\mathbf{x}}_k^\kappa \quad (15)$$

where $\mathbf{J}(\widehat{\mathbf{x}}_k^\kappa \boxminus \widehat{\mathbf{x}}_k^\kappa)$ is computed as below:

$$\mathbf{J}(\widehat{\mathbf{x}}_k^\kappa \boxminus \widehat{\mathbf{x}}_k^\kappa) = \begin{bmatrix} \mathbf{A}(\delta\theta_k)^{-T} & \mathbf{0}_{3 \times 15} \\ \mathbf{0}_{15 \times 3} & \mathbf{I}_{15 \times 15} \end{bmatrix}; \quad (16)$$

$$\delta\theta_k = {}^G\widehat{\mathbf{R}}_{I_k}^\kappa \boxminus {}^G\widehat{\mathbf{R}}_{I_k}$$

For the first iteration (i.e., the case of extended Kalman filter), $\widehat{\mathbf{x}}_k^\kappa = \widehat{\mathbf{x}}_k$, then $\mathbf{J} = \mathbf{I}$.

Combining this prior in (15) with (14) yields the maximum a-posteriori estimate (MAP):

$$\min_{\widetilde{\mathbf{x}}_k^\kappa} \left(\|\widetilde{\mathbf{x}}_k^\kappa\|_{\widehat{\mathbf{P}}_k^{-\frac{1}{2}}\mathbf{J}^T}^2 + \sum_{j=1}^m \|\mathbf{z}_j^\kappa + \mathbf{H}_j^\kappa \widetilde{\mathbf{x}}_k^\kappa\|_{\mathbf{R}_j^{-1}}^2 \right). \quad (17)$$

The result of (17) is a standard iterated Kalman filter [22, 26], which can be computed below (to simplify the notation, let $\mathbf{H} = \begin{bmatrix} \dots & \mathbf{H}_j^{\kappa T} & \dots \end{bmatrix}^T$, $\mathbf{P} = \mathbf{J}(\widehat{\mathbf{x}}_k^\kappa \boxminus \widehat{\mathbf{x}}_k^\kappa)^{-1} \widehat{\mathbf{P}}_k \mathbf{J}(\widehat{\mathbf{x}}_k^\kappa \boxminus \widehat{\mathbf{x}}_k^\kappa)^{-T}$, $\mathbf{R} = \text{diag}(\dots \mathbf{R}_j \dots)$, and $\mathbf{z}_k^\kappa = \begin{bmatrix} \dots & \mathbf{z}_j^\kappa & \dots \end{bmatrix}^T$)

$$\mathbf{K} = \mathbf{P}\mathbf{H}^T (\mathbf{H}\mathbf{P}\mathbf{H}^T + \mathbf{R})^{-1} \quad (18)$$

$$\widetilde{\mathbf{x}}_k^\kappa = -\mathbf{K}\mathbf{z}_k^\kappa \implies \widehat{\mathbf{x}}_k^{\kappa+1} = \widehat{\mathbf{x}}_k^\kappa \boxminus (-\mathbf{K}\mathbf{z}_k^\kappa)$$

The updated state estimate $\widehat{\mathbf{x}}_k^{\kappa+1}$ is then used to compute the residual in Section. III-C.3 and repeat the process until convergence. Assume the iteration stops at $\kappa + 1$, then the updated state is

$$\bar{\mathbf{x}}_k = \widehat{\mathbf{x}}_k^{\kappa+1}. \quad (19)$$

Moreover, the covariance of $\widehat{\mathbf{x}}_k^{\kappa+1}$ can be calculated as $(\mathbf{I} - \mathbf{K}\mathbf{H})\mathbf{P}$, which describes the covariance of the error between the ground-truth state \mathbf{x}_k and the state estimate at last iteration $\widehat{\mathbf{x}}_k^\kappa$ (i.e., $\mathbf{x}_k \boxminus \widehat{\mathbf{x}}_k^\kappa$). However, the covariance $\bar{\mathbf{P}}_k$

required for the next scan should be for $\widetilde{\mathbf{x}}_k \doteq \mathbf{x}_k \boxminus \bar{\mathbf{x}}_k$ (see (4)). To fill in the gap, we notice

$$\mathbf{x}_k \boxminus \widehat{\mathbf{x}}_k^\kappa = (\bar{\mathbf{x}}_k \boxminus \widetilde{\mathbf{x}}_k) \boxminus \widehat{\mathbf{x}}_k^\kappa = \mathbf{J}(\widehat{\mathbf{x}}_k^{\kappa+1} \boxminus \widehat{\mathbf{x}}_k^\kappa) \widetilde{\mathbf{x}}_k \quad (20)$$

where $\mathbf{J}(\widehat{\mathbf{x}}_k^{\kappa+1} \boxminus \widehat{\mathbf{x}}_k^\kappa)$ is defined in (16). Hence

$$\widetilde{\mathbf{x}}_k = \mathbf{J}^{-1} \cdot (\mathbf{x}_k \boxminus \widehat{\mathbf{x}}_k^\kappa), \quad (21)$$

and

$$\bar{\mathbf{P}}_k = \mathbf{J}^{-1} (\mathbf{I} - \mathbf{K}\mathbf{H}) \mathbf{P} \mathbf{J}^{-T}. \quad (22)$$

If the iterated Kalman filter fully converged, i.e., $\widehat{\mathbf{x}}_k^{\kappa+1} = \widehat{\mathbf{x}}_k^\kappa$, then $\mathbf{J} = \mathbf{I}$. The obtained state update (19) and covariance update (21) are ready to be used for the next scan.

A problem with the commonly used form in (18) is that it requires to invert the matrix $\mathbf{H}\mathbf{P}\mathbf{H}^T + \mathbf{R}$ which is in the dimension of the measurements. In practice, the number of LiDAR feature points are very large in number (e.g., more than 1,000 effective feature points in a scan), inverting a matrix of this size is prohibitive. As such, existing works [22, 26] only use a small number of measurements.

In this paper, we show that this limitation can be avoided. The intuition originates from (17) where the cost function is over the state, hence the solution should be calculated with complexity depending on the state dimension. In fact, if directly solving (17), we can obtain the same solution in (18) but with a new form of Kalman gain shown below:

$$\mathbf{K} = (\mathbf{H}^T \mathbf{R}^{-1} \mathbf{H} + \mathbf{P}^{-1})^{-1} \mathbf{H}^T \mathbf{R}^{-1}. \quad (23)$$

We prove in Appendix B that the two forms of Kalman gains are indeed equivalent based on the matrix inverse lemma [27]. Since the LiDAR measurements are independent, the covariance matrix \mathbf{R} is (block) diagonal and hence the new formula only requires to invert two matrix in the dimension of state in stead of measurements. The new formula greatly saves the computation as the state dimension is usually much lower than measurements in LIO.

D. Initialization

To obtain a good initial estimate of the system state (e.g., gravity vector ${}^G\mathbf{g}$, bias, and noise covariance) so to speedup the state estimator, an initialization is required. In FAST-LIO, the initialization is simple: keeping the LiDAR will static for several seconds. The collected data will be used to initialize the the IMU bias and the gravity vector. If non-repetitive scanning is supported by the LiDAR (e.g., Livox AIVA), keeping static also allows the LiDAR to capture a high-resolution initial map that is beneficial for the subsequent navigation.

IV. EXPERIMENT RESULTS

A. Computational Complexity Experiments

In order to validate the computational efficiency of the proposed new formula for computing Kalman gains. We intentionally replace the computation of Kalman gains by the old formula in our system and compare their computation time under the same system pipeline and number of feature

points. The results are shown in Fig. 4. It is obvious that the complexity of the new formula is much lower than the old one.

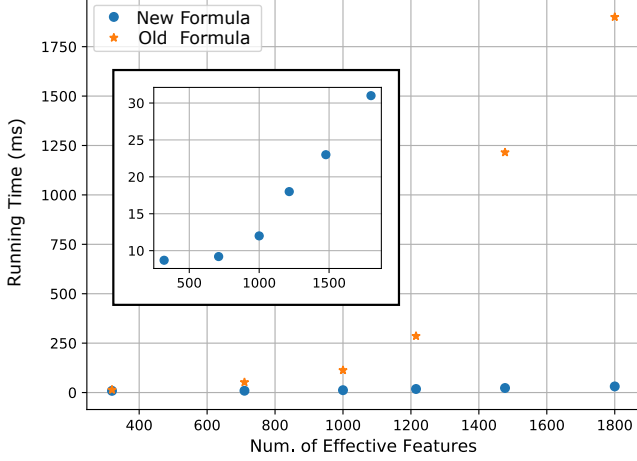


Fig. 4. The running time comparison between two Kalman gain computation methods.

B. UAV Flight Experiment

In order to validate the robustness and computational efficiency of FAST-LIO in actual mobile robots, we build a small-scale quadrotor which can carry a Livox Avia LiDAR with 70° FoV and a DJI Manifold 2-C onboard computer with a 1.8 GHz Intel i7-8550U CPU and 8 G RAM, as shown in Fig. 5. The UAV airframe have only 280 mm wheelbase and the LiDAR is directly installed on the airframe. The actual flight experiments show that FAST-LIO can achieve real-time and stable odometry output and mapping. The flight trajectory and mapping result is shown in Fig. 6. The average number of feature points and average running time is 1294 and 21 ms , also shown in Fig. 10. The drift in this experiment is smaller than 0.3% (0.051 m drift in 19 m trajectory).

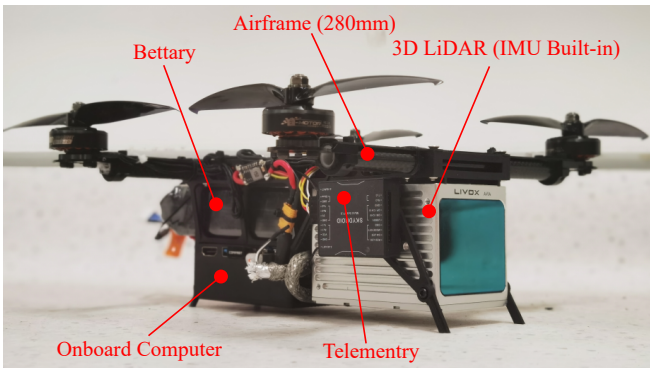


Fig. 5. The small-scale quadrotor platform carrying a Livox AVIA LiDAR and a DJI Manifold 2 onboard computer.

C. Indoor Experiments

Here we test FAST-LIO in a challenging indoor environment with large rotation speeds. To generate large move-

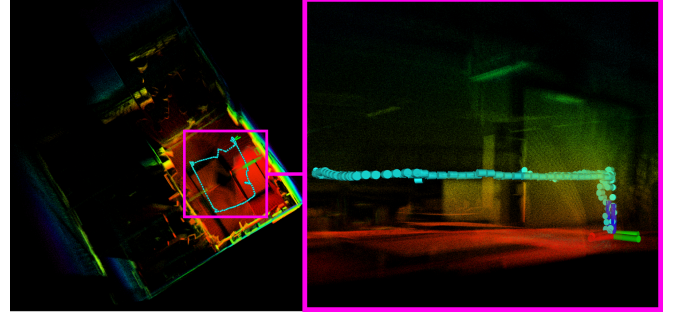


Fig. 6. During the flight, the UAV is under the control of a human pilot via RC, simulating a indoor exploration mission. The LiDAR-inertial odometry is sent to flight controller as the position and orientation feedback. After taking off from the ground, the UAV flies clockwise in a square shape while keeping at a constant 0.9 m height to explore the surroundings. In the end, the UAV lands at the take-off point. The drift before and after flight is hence used to evaluate the odometry drift and it is smaller than 0.3% . The flight video can be found in the same place with the code².

ments, the sensor suite is handheld. Fig. 8 shows the angular velocity and acceleration during the experiment. It is seen that the angular velocity often exceeds 100 deg/s . A state of the art implementation of LOAM on Livox LiDARs⁵ [9], LOAM with IMU⁶ [9], and LINS⁷ [22] are also tested as comparisons when the feature extraction are replaced with the one of FAST-LIO. The results shows that FAST-LIO can output odometry faster and stabler than others, as shown in Fig. 7 and Table. I. It should be noted that the LOAM+IMU is a loosely-coupled method, hence results in inconsistent mapping. The LINS package diverges from the beginning. This happens because the EKF formula in LINS package has high computational complexity (see Section. III-C-4)), so it randomly downsamples the feature points and segment the ground plane to decrease the measurement dimension. Since no obvious ground plane presents, the downsampled feature points lead to degeneration in this challenging indoor environment.

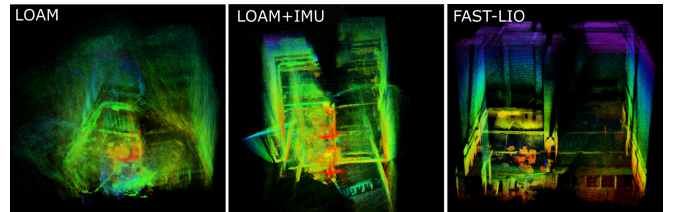


Fig. 7. The Mapping results of different LIO packages in an indoor environment with large rotation speed.

D. Outdoor Experiments

Here we show the performance of FAST-LIO in outdoor environments. Fig. 9 shows the mapping results of the Main Building in University of Hong Kong. The sensor suite is handheld during the data collection. The average processing

⁵https://github.com/Livox-SDK/livox_mapping

⁶https://github.com/Livox-SDK/livox_horizon_loam

⁷<https://github.com/ChaoqinRobotics/LINS—LiDAR-inertial-SLAM>

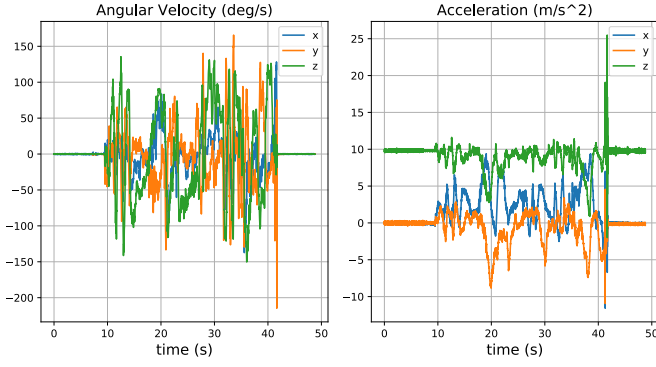


Fig. 8. The angular velocity and acceleration in the indoor experiments.

TABLE I
COMPARISON OF LIO PACKAGES PROCESSING A LiDAR SCAN

Packages	Num. of effective features	Running time
LOAM	1107	59 <i>ms</i>
LOAM+IMU	1107	44 <i>ms</i>
LINS	210	Null
FAST-LIO	1430	23 <i>ms</i>

time of a scan is 23 *ms* with average. Further, we also summarize the number of feature points and running time of the above UAV experiment and indoor experiment in Fig. 10. It should be noted that the FAST-LIO is real-time running in the DJI Manifold2 onboard computer for all the experiments.

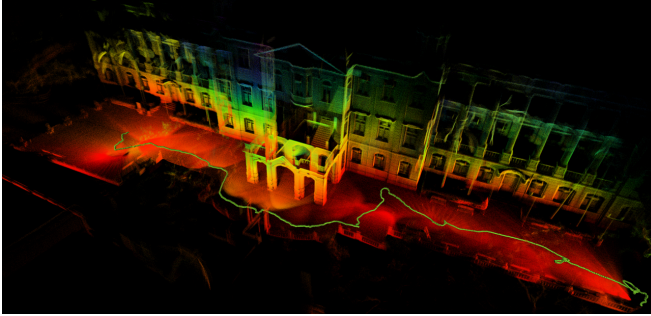


Fig. 9. Mapping results of the Main Building, University of Hong Kong.

V. CONCLUSION

This paper proposed FAST-LIO, a computationally efficient and robust LiDAR-inertial odometry framework by tightly-coupled iterated Kalman filter. We used the forward and backward propagation to predict the states and compensate for the motion in a LiDAR scan. Besides, we proved and implemented an equivalent formula that can achieve much lower complexity for the Kalman gain computation. FAST-LIO was tested in the UAV flight experiment, challenging indoor environment with large rotation speed and outdoor environment. In all tests, our method produced precise, real-time and reliable navigation results.

APPENDIX

A. Computation of $\mathbf{F}_{\tilde{\mathbf{x}}}$ and $\mathbf{F}_{\mathbf{w}}$

Recall $\mathbf{x}_i = \hat{\mathbf{x}}_i \boxplus \tilde{\mathbf{x}}_i$, denote $\mathbf{g}(\tilde{\mathbf{x}}_i, \mathbf{w}_i) = \mathbf{f}(\mathbf{x}_i, \mathbf{u}_i, \mathbf{w}_i)\Delta t = \mathbf{f}(\hat{\mathbf{x}}_i \boxplus \tilde{\mathbf{x}}_i, \mathbf{u}_i, \mathbf{w}_i)\Delta t$. Then the error state

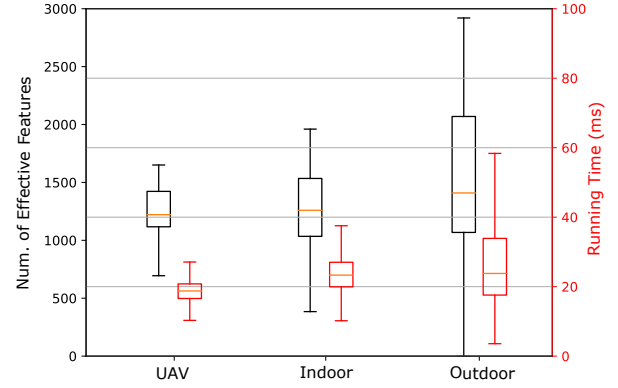


Fig. 10. Summary of the effective feature number and running time in the above UAV experiment, indoor experiment and outdoor experiments.

model (6) is rewritten as:

$$\tilde{\mathbf{x}}_{i+1} = \underbrace{((\hat{\mathbf{x}}_i \boxplus \tilde{\mathbf{x}}_i) \boxplus \mathbf{g}(\tilde{\mathbf{x}}_i, \mathbf{w}_i)) \boxminus (\hat{\mathbf{x}}_i \boxplus \mathbf{g}(\mathbf{0}, \mathbf{0}))}_{\mathbf{G}(\tilde{\mathbf{x}}_i, \mathbf{g}(\tilde{\mathbf{x}}_i, \mathbf{w}_i))} \quad (24)$$

Following the chain rule of partial differentiation, the matrix $\mathbf{F}_{\tilde{\mathbf{x}}}$ and $\mathbf{F}_{\mathbf{w}}$ in (6) are computed as below.

$$\begin{aligned} \mathbf{F}_{\tilde{\mathbf{x}}} &= \left. \frac{\partial \mathbf{G}(\tilde{\mathbf{x}}_i, \mathbf{g}(\tilde{\mathbf{x}}_i, \mathbf{0}))}{\partial \tilde{\mathbf{x}}_i} \right|_{\tilde{\mathbf{x}}_i=\mathbf{0}} \\ &= \left(\frac{\partial \mathbf{G}(\tilde{\mathbf{x}}_i, \mathbf{g}(\mathbf{0}, \mathbf{0}))}{\partial \tilde{\mathbf{x}}_i} + \frac{\partial \mathbf{G}(\mathbf{0}, \mathbf{g}(\tilde{\mathbf{x}}_i, \mathbf{0}))}{\partial \mathbf{g}(\tilde{\mathbf{x}}_i, \mathbf{0})} \frac{\partial \mathbf{g}(\tilde{\mathbf{x}}_i, \mathbf{0})}{\partial \tilde{\mathbf{x}}_i} \right) \Big|_{\tilde{\mathbf{x}}_i=\mathbf{0}} \\ \mathbf{F}_{\mathbf{w}} &= \left. \frac{\partial \mathbf{G}(\mathbf{0}, \mathbf{g}(\mathbf{0}, \mathbf{w}_i))}{\partial \mathbf{w}_i} \right|_{\mathbf{w}_i=\mathbf{0}} \\ &= \left(\frac{\partial \mathbf{G}(\mathbf{0}, \mathbf{g}(\mathbf{0}, \mathbf{w}_i))}{\partial \mathbf{g}(\mathbf{0}, \mathbf{w}_i)} \frac{\partial \mathbf{g}(\mathbf{0}, \mathbf{w}_i)}{\partial \mathbf{w}_i} \right) \Big|_{\mathbf{w}_i=\mathbf{0}} \end{aligned} \quad (25)$$

For the sake of readability, we hide the $|\tilde{\mathbf{x}}_i=\mathbf{0}$ and $|\mathbf{w}_i=\mathbf{0}$, then all the partial differentials in (25) are computed as below.

$$\begin{aligned} \frac{\partial \mathbf{G}(\tilde{\mathbf{x}}_i, \mathbf{g}(\mathbf{0}, \mathbf{0}))}{\partial \tilde{\mathbf{x}}_i} &= \begin{bmatrix} \text{Exp}(-\hat{\boldsymbol{\omega}}_i \Delta t) & \mathbf{0} \\ \mathbf{0} & \mathbf{I}_{15} \end{bmatrix} \\ \frac{\partial \mathbf{G}(\mathbf{0}, \mathbf{g}(\tilde{\mathbf{x}}_i, \mathbf{0}))}{\partial \mathbf{g}(\tilde{\mathbf{x}}_i, \mathbf{0})} &= \frac{\partial \mathbf{G}(\mathbf{0}, \mathbf{g}(\mathbf{0}, \mathbf{w}_i))}{\partial \mathbf{g}(\mathbf{0}, \mathbf{w}_i)} \\ &= \begin{bmatrix} \mathbf{A}(\hat{\boldsymbol{\omega}}_i \Delta t)^T & \mathbf{0} \\ \mathbf{0} & \mathbf{I}_{15} \end{bmatrix} \\ \frac{\partial \mathbf{g}(\tilde{\mathbf{x}}_i, \mathbf{0})}{\partial \tilde{\mathbf{x}}_i} &= \frac{\partial \mathbf{f}(\tilde{\mathbf{x}}_i \boxplus \tilde{\mathbf{x}}_i, \mathbf{u}_i, \mathbf{0})}{\partial \tilde{\mathbf{x}}_i} \Delta t \\ &= \begin{bmatrix} \mathbf{0} & \mathbf{0} & \mathbf{0} & -\mathbf{I}_3 & \mathbf{0} & \mathbf{0} \\ \mathbf{0} & \mathbf{0} & \mathbf{0} & \mathbf{I}_3 & \mathbf{0} & \mathbf{0} \\ -{}^G\hat{\mathbf{R}}_{I_i}[\hat{\mathbf{a}}_i]_{\wedge} & \mathbf{0} & \mathbf{0} & \mathbf{0} & -{}^G\hat{\mathbf{R}}_{I_i} & \mathbf{I}_3 \\ \mathbf{0} & \mathbf{0} & \mathbf{0} & \mathbf{0} & \mathbf{0} & \mathbf{0} \\ \mathbf{0} & \mathbf{0} & \mathbf{0} & \mathbf{0} & \mathbf{0} & \mathbf{0} \\ \mathbf{0} & \mathbf{0} & \mathbf{0} & \mathbf{0} & \mathbf{0} & \mathbf{0} \end{bmatrix} \Delta t \\ \frac{\partial \mathbf{g}(\mathbf{0}, \mathbf{w}_i)}{\partial \mathbf{w}_i} &= \frac{\partial \mathbf{f}(\tilde{\mathbf{x}}_i, \mathbf{u}_i, \mathbf{w}_i)}{\partial \mathbf{w}_i} \Delta t \\ &= \begin{bmatrix} -\mathbf{I}_3 & \mathbf{0} & \mathbf{0} & \mathbf{0} \\ \mathbf{0} & \mathbf{0} & \mathbf{0} & \mathbf{0} \\ \mathbf{0} & -{}^G\hat{\mathbf{R}}_{I_i} & \mathbf{0} & \mathbf{0} \\ \mathbf{0} & \mathbf{0} & \mathbf{I}_3 & \mathbf{0} \\ \mathbf{0} & \mathbf{0} & \mathbf{0} & \mathbf{I}_3 \\ \mathbf{0} & \mathbf{0} & \mathbf{0} & \mathbf{0} \end{bmatrix} \Delta t \end{aligned}$$

where is introduced in [28] and $\hat{\boldsymbol{\omega}}_i = \boldsymbol{\omega}_{m_i} - \hat{\mathbf{b}}_{\boldsymbol{\omega}_i}$, $\hat{\mathbf{a}}_i =$

$\mathbf{a}_{m_i} - \hat{\mathbf{b}}_{\mathbf{a}_i}$ and $\mathbf{A}(\mathbf{u})^{-1}$ is computed as below.

$$\mathbf{A}(\mathbf{u})^{-1} = \mathbf{I} - \frac{1}{2}[\mathbf{u}]_{\wedge} + (1 - \alpha(\|\mathbf{u}\|)) \frac{[\mathbf{u}]_{\Delta}^2}{\|\mathbf{u}\|^2}$$

$$\alpha(m) = \frac{m}{2} \cot\left(\frac{m}{2}\right) = \frac{m \cos(m/2)}{2 \sin(m/2)}$$

B. Equivalent Kalman Gain formula

Based on the matrix inverse lemma [27], we can get:

$$(\mathbf{P}^{-1} + \mathbf{H}^T \mathbf{R}^{-1} \mathbf{H})^{-1} = \mathbf{P} - \mathbf{P} \mathbf{H}^T (\mathbf{H} \mathbf{P} \mathbf{H}^T + \mathbf{R})^{-1} \mathbf{H} \mathbf{P}$$

Substituting above into (23), we can get:

$$\begin{aligned} \mathbf{K} &= (\mathbf{H}^T \mathbf{R}^{-1} \mathbf{H} + \mathbf{P}^{-1})^{-1} \mathbf{H}^T \mathbf{R}^{-1} \\ &= \mathbf{P} \mathbf{H}^T \mathbf{R}^{-1} - \mathbf{P} \mathbf{H}^T (\mathbf{H} \mathbf{P} \mathbf{H}^T + \mathbf{R})^{-1} \mathbf{H} \mathbf{P} \mathbf{H}^T \mathbf{R}^{-1} \end{aligned} \quad (26)$$

Now note that $\mathbf{H} \mathbf{P} \mathbf{H}^T \mathbf{R}^{-1} = (\mathbf{H} \mathbf{P} \mathbf{H}^T + \mathbf{R}) \mathbf{R}^{-1} - \mathbf{I}$. Substituting it into (26), we can get the standard Kalman gain formula in (18), as shown below.

$$\begin{aligned} \mathbf{K} &= \mathbf{P} \mathbf{H}^T \mathbf{R}^{-1} - \mathbf{P} \mathbf{H}^T \mathbf{R}^{-1} + \mathbf{P} \mathbf{H}^T (\mathbf{H} \mathbf{P} \mathbf{H}^T + \mathbf{R})^{-1} \\ &= \mathbf{P} \mathbf{H}^T (\mathbf{H} \mathbf{P} \mathbf{H}^T + \mathbf{R})^{-1}. \quad \blacksquare \end{aligned}$$

REFERENCES

- [1] K. Sun, K. Mohta, B. Pfrommer, M. Watterson, S. Liu, Y. Mulgaonkar, C. J. Taylor, and V. Kumar, "Robust stereo visual inertial odometry for fast autonomous flight," *IEEE Robotics and Automation Letters*, vol. 3, no. 2, pp. 965–972, 2018.
- [2] A. Howard, "Real-time stereo visual odometry for autonomous ground vehicles," in *2008 IEEE/RSJ International Conference on Intelligent Robots and Systems*. IEEE, 2008, pp. 3946–3952.
- [3] T. Qin, P. Li, and S. Shen, "Vins-mono: A robust and versatile monocular visual-inertial state estimator," *IEEE Transactions on Robotics*, vol. 34, no. 4, pp. 1004–1020, 2018.
- [4] C. Forster, M. Pizzoli, and D. Scaramuzza, "Svo: Fast semi-direct monocular visual odometry," in *2014 IEEE international conference on robotics and automation (ICRA)*. IEEE, 2014, pp. 15–22.
- [5] D. Wang, C. Watkins, and H. Xie, "Mems mirrors for lidar: A review," *Micromachines*, vol. 11, no. 5, p. 456, 2020.
- [6] Z. Liu, F. Zhang, and X. Hong, "Low-cost retina-like robotic lidars based on incommensurable scanning," *arXiv preprint arXiv:2006.11034*, 2020.
- [7] P. J. Besl and N. D. McKay, "Method for registration of 3-d shapes," in *Sensor fusion IV: control paradigms and data structures*, vol. 1611. International Society for Optics and Photonics, 1992, pp. 586–606.
- [8] A. Segal, D. Haehnel, and S. Thrun, "Generalized-icp," in *Robotics: science and systems*, vol. 2, no. 4. Seattle, WA, 2009, p. 435.
- [9] J. Zhang and S. Singh, "Loam: Lidar odometry and mapping in real-time," in *Robotics: Science and Systems*, vol. 2, no. 9, 2014.
- [10] T. Shan and B. Englot, "Lego-loam: Lightweight and ground-optimized lidar odometry and mapping on variable terrain," in *2018 IEEE/RSJ International Conference on Intelligent Robots and Systems (IROS)*. IEEE, 2018, pp. 4758–4765.
- [11] J. Lin and F. Zhang, "LoamLivox: A fast, robust, high-precision lidar odometry and mapping package for lidars of small fov," *arXiv preprint arXiv:1909.06700*, 2019.
- [12] W. Zhen, S. Zeng, and S. Soberer, "Robust localization and localizability estimation with a rotating laser scanner," in *2017 IEEE International Conference on Robotics and Automation (ICRA)*. IEEE, 2017, pp. 6240–6245.
- [13] Y. Balazadegan Sarvrood, S. Hosseinyalamdary, and Y. Gao, "Visual-lidar odometry aided by reduced imu," *ISPRS international journal of geo-information*, vol. 5, no. 1, p. 3, 2016.
- [14] X. Zuo, P. Geneva, W. Lee, Y. Liu, and G. Huang, "Lic-fusion: Lidar-inertial-camera odometry," *arXiv preprint arXiv:1909.04102*, 2019.
- [15] P. Geneva, K. Eickenhoff, Y. Yang, and G. Huang, "Lips: Lidar-inertial 3d plane slam," in *2018 IEEE/RSJ International Conference on Intelligent Robots and Systems (IROS)*. IEEE, 2018, pp. 123–130.
- [16] C. Forster, L. Carlone, F. Dellaert, and D. Scaramuzza, "On-manifold preintegration for real-time visual-inertial odometry," *IEEE Transactions on Robotics*, vol. 33, no. 1, pp. 1–21, 2016.
- [17] M. Hsiao, E. Westman, and M. Kaess, "Dense planar-inertial slam with structural constraints," in *2018 IEEE International Conference on Robotics and Automation (ICRA)*. IEEE, 2018, pp. 6521–6528.
- [18] H. Ye, Y. Chen, and M. Liu, "Tightly coupled 3d lidar inertial odometry and mapping," in *2019 International Conference on Robotics and Automation (ICRA)*. IEEE, 2019, pp. 3144–3150.
- [19] A. Bry, A. Bachrach, and N. Roy, "State estimation for aggressive flight in gps-denied environments using onboard sensing," in *2012 IEEE International Conference on Robotics and Automation*. IEEE, 2012, pp. 1–8.
- [20] J. A. Hesch, F. M. Mirzaei, G. L. Mariottini, and S. I. Roumeliotis, "A laser-aided inertial navigation system (l-ins) for human localization in unknown indoor environments," in *2010 IEEE International Conference on Robotics and Automation*. IEEE, 2010, pp. 5376–5382.
- [21] Z. Cheng, D. Liu, Y. Yang, T. Ling, X. Chen, L. Zhang, J. Bai, Y. Shen, L. Miao, and W. Huang, "Practical phase unwrapping of interferometric fringes based on unscented kalman filter technique," *Optics express*, vol. 23, no. 25, pp. 32 337–32 349, 2015.
- [22] C. Qin, H. Ye, C. E. Pranata, J. Han, S. Zhang, and M. Liu, "Lins: A lidar-inertial state estimator for robust and efficient navigation," *arXiv preprint arXiv:1907.02233*, 2019.
- [23] M. Raitoharju and R. Piché, "On computational complexity reduction methods for kalman filter extensions," *IEEE Aerospace and Electronic Systems Magazine*, vol. 34, no. 10, pp. 2–19, 2019.
- [24] C. Hertzberg, R. Wagner, U. Frese, and L. Schröder, "Integrating generic sensor fusion algorithms with sound state representations through encapsulation of manifolds," *Information Fusion*, vol. 14, no. 1, pp. 57–77, 2013.
- [25] W. Xu, D. He, Y. Cai, and F. Zhang, "Robots state estimation and observability analysis based on statistical motion models," 2020.
- [26] M. Bloesch, M. Burri, S. Omari, M. Hutter, and R. Siegwart, "Iterated extended kalman filter based visual-inertial odometry using direct photometric feedback," *The International Journal of Robotics Research*, vol. 36, no. 10, pp. 1053–1072, 2017.
- [27] N. J. Higham, *Accuracy and stability of numerical algorithms*. SIAM, 2002.
- [28] F. Bullo and R. M. Murray, "Proportional derivative (pd) control on the euclidean group," in *European control conference*, vol. 2, 1995, pp. 1091–1097.